The construction of turbulent flow through submerged flexible vegetation

[1]BHABANI SANKAR SI,
Gandhi Institute of Excellent Technocrats, Bhubaneswar, India
[2]PRADOSH MOHANTY,
Mahavir Institute of Engineering and Technology, Bhubaneswar, Odisha, India

Abstract: The hydrodynamics of violent course through lowered adaptable vegetation is researched in a flume utilizing acoustic Doppler velocimetery (ADV) estimations. The stream attributes, for example, the energetics and force move got from regular otherworldly and quadrant examinations are considered as the stream experiences a limited vegetation fix. Steady with various shade stream tests, a shear layer and intelligible vortex structures close to the overhang top arise brought about by Kelvin–Helmholtz hazards after the stream equilibrates with the vegetated layer. These hazards are usually ascribed to speed contrasts between non-vegetated a lot shelter layers in concurrence with various analyses and recreations led on thick unbending overhangs. The force ghastly thickness work for vertical speed tempestuous vacillations at various downstream positions beginning from the edge of the vegetation layer are likewise registered. For a preset water profundity, the prevailing dimensionless recurrence is discovered to be shockingly invariant around 0.027 notwithstanding huge contrasts in vegetation densities. The discharge and clear occasions altogether add to the Reynolds stresses close to the highest point of the vegetation. The energy transition conveyed by discharges is bigger than its partner conveyed by the ranges over the covering top. Notwithstanding, the energy transition conveyed by clears is bigger beneath the highest point of the covering.

Key words: Artificial flexible vegetation, coherent vortex structures, drag force, open channel flow, velocity distribution

Introduction

With rapid urbanization and industrialization, water quality in rivers and streams is becoming seriously polluted resulting in gradual degradation of ecosystem services. How to restore such degraded or damaged ecosystems and effectively control the deteriorating water quality is becoming a major research issue of societal significance[1-2]. Ecological restoration of rivers and streams is concerned with eco-hydraulics and ecological engineering so as to ensure optimal flow conditions needed to sustain a resilient food-web[3-4]. The engineering concerns include ecological bank and slope protection and flow regulation. Aquatic vegetation is an intrinsic part of such efforts given its role in purifying water through absorption and microbial metabolism [5]. In fact, phytoremediation is now widely used in river and wetland water treatment and remains key to many restoration projects[6].

While few dispute the ecological significance of water movement through vegetation, describing such complex flow remains a daunting task[7-9]. All ecological restoration measures, including nutrient and contaminant transport[10-11], require description of flow through vegetation. In particular, non-uniform flow through vegetated sections is becoming a necessary first step when addressing the many

---

engineering challenges for the following reasons:

(1) Aquatic plants can resist water flushing, protect the river bank slope and maintain the riverbed stability.

(2)The stems, the leaves and the epidermis of aquatic plants have strong absorption capacity that can purify water through biochemical and physical methods[12]. Emergent vegetation can fix nitrogen and phosphorus through microbial metabolism and self-absorption, which is often used in wetland restoration[13]. (3) Aquatic vegetation provides an attachment matrix and a habitat for aquatic organisms, thus playing an active role in the maintenance and protection of biological diversity. Hence, it can be surmised that restoration or design of aquatic ecosystems and wetlands[14-19] must confront all the complications encountered as turbulent flows traverse a vegetated section. The work here primarily deals with the effects of vegetation on the increased flow resistance, the reduced bulk velocity, and the generation of wakes and other coherent eddies that transport nutrients or sediments. To be clear, studies of flow through and above vegetated canopies is by no means a new topic. It was studied for well over 60 years in both terrestrial and aquatic environments[20-26] and continues to draw significant research attention today. Reviewing all this literature is well outside the scope here; however, salient features about key theories, experiments, and simulations most pertinent to the study objectives are covered next.

In terrestrial and several aquatic systems, the case of rigid vegetation immersed in a deep fully developed turbulent boundary layer has been Considered, where the vegetation height is much smaller than the boundary layer height. The flow through aquatic vegetation differs from their terrestrial counterpart in that the water depth can be smaller (i.e., emergent vegetation) or larger (i.e., submerged vegetation) than the vegetation height[27-28]. Moreover, the multi-scaled nature of vegetation as well as flexibility further increases the complexity of such flows. Nonetheless, for steady-uniform flow over submerged rigid vegetation, a number of features were revealed using Reynolds-averaged Navier-Stokes (RANS) budgets [29-30]. The water depth can be divided into three distinct layers labelled as (1) the vegetation layer, dominated by wakes resembling Karman vortex streets, (2) the shear layer, dominated by Kelvin-Helmholtz (K-H) instabilities, and (3) a non-vegetation layer resembling a canonical rough-wall boundary layer, where attached eddies dominate the mixing length for momentum exchange. Numerous experiments on dense canopies reporting mean and turbulent flow properties suggest that: (1) The mean velocity profile is characterized by an inflection point near the canopy top, spawning vortices that resemble K-H instabilities. These vortices topologically differ from attached eddies dominating canonical turbulent boundary layers. (2) The second-order flow statistics all exhibit some attenuation with reduced depth inside the canopy. (3) While both ejections and sweeps contribute to momentum transport, sweeps contribute more than ejections to the overall momentum flux in virtually all layers inside canopies. (4) The spectral shapes of the velocity components are impacted by two new processes that are entirely absent in canonical boundary layers: (a) the work that the mean flow exercises against the foliage drag and produces turbulent kinetic energy by wakes and (b) the short-circuiting of the energy cascade representing the same physical process but acting on turbulent eddies rather than on the mean flow[31-34]. The flow is partly blocked by vegetation and the fluid-solid interaction is often represented by a drag force with an associated drag coefficient. Unsurprisingly, there are several models representing such drag effect including the drag coefficient for an isolated cylinder, the bulk drag coefficient for an array of cylinders and an explicit vertically variable local drag coefficient[35-37]. In addition to this “vertical” picture, flows in natural rivers also encounter a discontinuous vegetation patch of a finite length. This additional length scale makes the problem of describing flow statistics within and above vegetation difficult because multiple horizontal and vertical length scales must be simultaneously considered.

Laboratory experiments have previously contributed data to the development of theories for such complex flows and are the main tools to be employed here[38-42]. In laboratory experiments, the water level and/or the vegetation density must vary as control parameters. The experiments reported here also consider flexible vegetation with a range of flexibility commensurate with those encountered in natural settings[43-51]. For finite vegetation patches, longitudinal advection affects momentum and mass transport in a zone where the flow first encounters the patch and equilibration with vegetation has not fully occurred[52-53]. Okamoto and Nezu[54] performed early seminal experiments in an open channel covered by rigid submerged vegetation to investigate the transition process from a boundary layer (prior to the vegetation patch) to a mixing layer (after the flow equilibrated with the vegetation patch) along the flow direction. They proposed a model composed of four zones, namely, the smooth river bed, the diverging flow, the development, and the completely developed zones. These experiments, while beginning to shift the studies of canopy turbulence from 1-D (mainly vertical) to 2-D (vertical and horizontal), do not capture the complexity encountered in natural streams or wetlands. How flexible vegetation with complex morphology alter the emerging picture put forth by Okamoto and Nezu is the main concern of this paper. Flow through uniform flexible vegetation was the focus of several prior studies[36, 55-59] as briefly reviewed next. Compared with the rigid vegetation that remains erect, flexible vegetation exhibits certain movement and bending under the influence of water flow. Fathi-Maghadam[48] experimentally showed that flow within flexible vegetation with different shapes differ from their rigid counterparts and that such vegetation attributes cannot be ignored when characterizing flow statistics. Through experiments on uniform flow, Kouwen[60-61] also showed that different vegetation characteristics such as vegetation density and shape, flexibility and flow velocity change the bending degree of flexible vegetation and subsequent frictional losses. Jarvela[62] evaluated the relation between different types of flexible plants and the so-called Darcy-Weisbach resistance coefficient, the relative roughness, the average cross-section velocity, and the water depth and reported that the friction factor is decreased with increased Reynolds number, except in a series of leafless willows on a bare bottom soil, for which the friction was more or less independent of the Reynolds number. From those experiments, it is concluded that the plant rigidity does affect the Darcy-Weisbach friction factor, which cannot be ignored. Ghisalberti and Nepf[63] compared two flow characteristics for the upright state and the *monami* phenomenon of flexible vegetation and investigated the effects of the vegetation flexibility on the flow structure. The coupling effect between the vegetation and water flow reduces the drag force of the vegetation and increases the flow velocity and the turbulent stress. That is, vegetation deflection may be a passive “drag-reduction” strategy employed by vegetation. Righetti[64] conducted experiments in an open channel covered by two kinds of flexible bushes of different densities. They found that the net upward momentum flux and the associated suspended mass transport flux decrease with increases in bush density. Nepf and Vivoni[65] evaluated a flow through flexible vegetation of limited water depth. They divided the flow in the vegetation layer into a vertical exchange zone, located near the top of a vegetation, and a longitudinal exchange zone, located below the vertical exchange zone. The shear layer generated at the top of the vegetation causes the water in the vertical zone to have a strong vertical turbulent exchange with the non-vegetation layer. The flow in the longitudinal exchange zone is similar to the flow around the cylinder[66] and experiences advection relative to the surrounding water body. Interestingly, the same experiments suggest only a vertical exchange zone exists in the non-submerged vegetation.

In the last three decades, flow through vegetated patches were analyzed using both Reynolds averaged Navier-Stokes equations or RANS and large eddy simulations or LES[67-70]. In RANS, different discrete methods to iteratively solve the three main flow equations, i.e., the mean continuity equation, the mean momentum equation and the turbulence kinetic energy equation have been proposed. The main issues here are how to represent the vegetation patch and its effects on the flow for modeling or simulation purposes.

Rowiński et al.[71] investigated water flow within non-submerged rigid vegetation using a mixing length model, which treats vegetation as a drag force with prescribed drag coefficient. Noat et al.[72] applied a three-dimensional turbulent algebraic stress model to investigate flow in riparian vegetation using similar approaches to RANS. Using LES, Mattis et al.[73] derived a macroscale vegetation resistance model for high Reynolds number flows and showed how sub-grid scale effects may be represented in LES. Zhang et al.[74] studied the interaction between wave, current, and vegetation by numerical approaches and proposed an explicit depth-averaged hydrodynamic model coupled with a wave spectral model (CMS-wave) to represent wave and wave-induced currents in coastal waters. Su et al.[45] conducted an LES for vegetation flow to assess how variations in water depth impact flow through vegetation. Fischer-Antze et al.[75] numerically solved the RANS equations using the SIMPLE algorithm along with a k - ε turbulence model for cylindrical vegetation and showed how to optimally parameterize the effects of vegetation in such k - ε modeling. Wang et al.[76] adopted a 3-D hydrodynamic model with an additional hydraulic resistance for aquatic plants. The numerical model was used for South-North Water Diversion in the Nansi Lake. Their results showed that their proposed hydraulic resistance for aquatic plants is feasible with a calculation error less than 15%.

The work here focuses on differences between turbulent flow through rigid vegetation and flexible vegetation characterized by vertically non-uniform plant area density. Sedge was selected to allow for the influence of rigidity to be controlled. The flow characteristics to be considered are the shape of the mean velocity profile, the attenuation of the second-order statistics within the canopy, the relative significance of ejections and sweeps, the spectral shapes of the vertical velocity, and the development of the shear layer longitudinally as the flow adjusts to the presence of flexible vegetation. The sedge is a grass-like flexible plant with an irregular leaf area shape characterized by an approximate triangular stem and an inconspicuous flower. Hence, its morphology

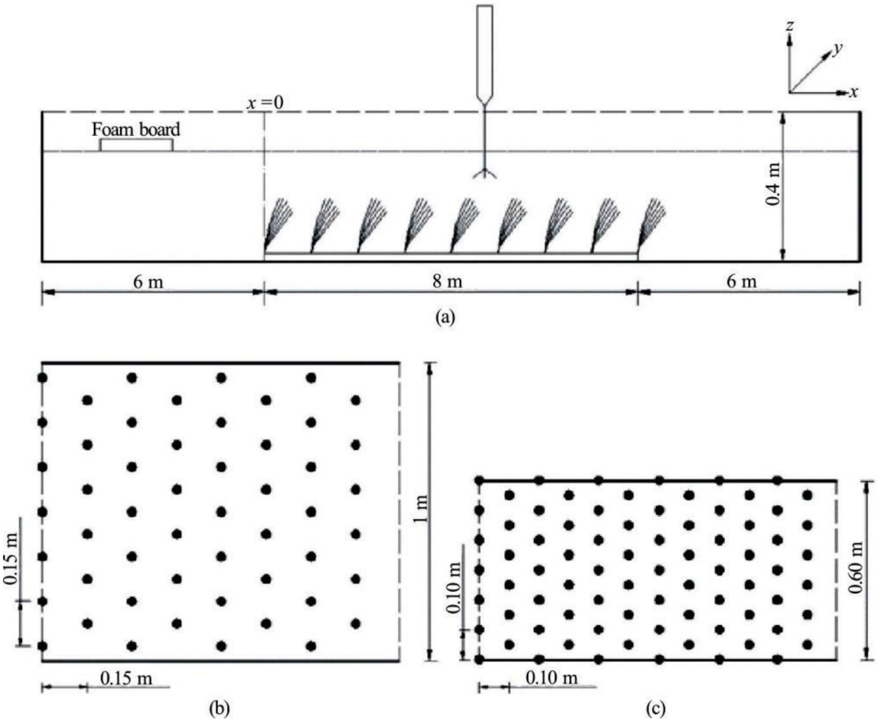

Fig. 1 The experimental setup and vegetation placement in a rectangular channel (the layout is not to the scale) showing the longitudinal (a), plane (b) and cross-sectional (c) views. The *z* is the distance from the bottom of the channel, and h_v is the deflected height of the vegetation and *b* is the lateral spacing between vegetation elements whereas *l* is the longitudinal spacing. The vegetation element placement is shown in panels (b) and (c).

deviates appreciably from "slender" cylinders used in prior studies. The experiments are conducted to clarify how the Okamoto and Nezu picture is altered because of non-uniformity in plant area density and plant rigidity. It is envisaged that the results from the flume experiments here provide a benchmark reference data set to be employed in testing future numerical models and simulations. It is a unique data set because the flow is stationary, high Reynolds number, non-uniform in the longitudinal and vertical directions, and wide ranging vegetation rigidity are featured that impact the flow statistics.

1. Experiments

The experiments are conducted using two glass channels at the State Key Laboratory of Water Resources and Hydropower Engineering Science in Wuhan University, China. The two channels are both 20 m long. One of the channels has a cross-section of 0.6 m×0.4 m with a 0.04% bed slope $(= S)$, and the other has a cross-section of 1.0 m×0.4 m with $S = 0.01\%$. The discharge is controlled by an electro-magnetic flow meter installed at the start of the channel, and the water level is adjusted by a tailgate located at the end of the channels. The total length of the vegetation zone is 8 m to ensure a complete development of the flow within and above the vegetation zone. The distance between the inlets of the flume and the vegetation zone is 6 m. The layout of the experimental device is shown in Fig. 1. The vegetation, fixed on a perforated board with wire and glass glue, is in a staggered arrangement, as shown in

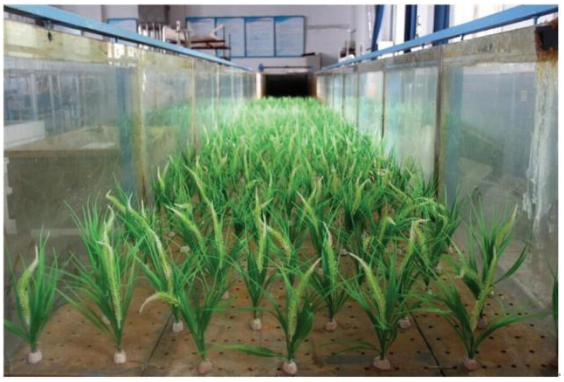

Fig. 2 (Color online) Arrangement of the plastic model plants representing the sedge.

Fig. 2. The velocity measurements are conducted after the flow reaches steady state conditions. The velocity profiles are measured using an acoustic Doppler velocimeter (ADV), placed at the mid-perpendicular line of two vegetation rows, which can be laterally moved. Each vertical line has 25-35 measuring points, and the vertical distance between two measuring points is 0.005 m-0.010 m. The sampling frequency and the measuring time of the ADV are 50 Hz and 120 s, respectively, resulting in 6000 instantaneous velocities for each measuring point.

Previous studies employed glass rods or Polyvinyl chloride (PVC) thin blades of regular shapes to represent the vegetation in rivers. However, real vegetation are flexible and irregular, and are far from the “niceties” of slender rods. Therefore, a meadow model plant is used to represent the natural vegetation (sedge shape). Each model plant has 11 plastic slips and the diameter of the trunk is approximately 0.015 m. The average height of the sedge meadow model is 0.210 m and the lateral and longitudinal spread widths of the slip are approximately 0.170 m, 0.045 m, respectively. The 11 plastic slips are individually fixed to a 0.01 m-thick ceramic elliptical bottom as shown in Fig. 3. The model plants have a certain degree of flexibility and can swing when the water flows through them. These model plants are suitable to represent the sedge because they do not have large deformation or bending.

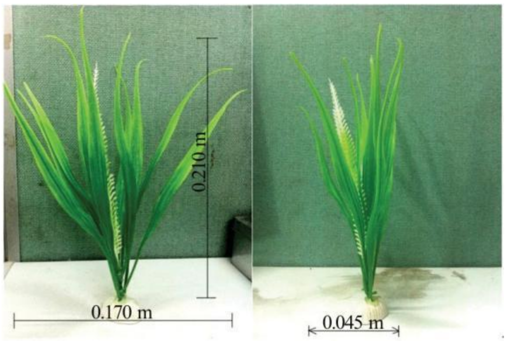

Fig. 3 (Color online) Photograph of the sedge vegetation model used in the experiments

The experiments are conducted for 3 different plant densities and water depth conditions. These experimental parameters are summarized in Table 1, where n is the number of plants in a unit area, b is the lateral distance between two adjacent model plants, l is the longitudinal distance between two nearby plants, H is the water depth, and u is the time- and cross-sectionally averaged velocity and can be calculated as $u = Q/(B \times H)$, where Q is the flow rate, and B is the total width of the channel. Meanwhile, h_v is the real average height of each plant after bending is accounted for. The width to depth ratio is expressed as B / H and varies by a factor of 2 (1.8-3.7). The Froude and Reynolds numbers covered by the experiments are 0.061-0.080, 15 008-18 127 respectively.

2. Results and discussions

The results are organized as follows: the influence of flexible submerged vegetation on the mean flow is first considered (Section 2.1) followed by its effect on the turbulent structure (Sections 2.2, 2.3). Next, the propagation frequency of the vortices and the dominant flow pattern in the submerged-vegetated flow are computed and reported.

Throughout, the data presentation convention is as follows: The vertical distances (or z) are normalized by h_v and the longitudinal distances (or x) are normalized by the total longitudinal length of the vegetation zone model $(L_v = 8\text{ m})$. The velocities are normalized by the local depth-averaged velocity (U_m), and the Reynolds stresses are normalized by the friction velocity $u_* = [(-\overline{u'w'})_{\max}]^{1/2}$.

2.1 *Influence of flexible submerged vegetation on the mean flow*

The main resistance to the flow is from the vegetation. The distributed drag force associated with the vegetation is shown to be much greater than the ground stresses as discussed elsewhere[36, 77]. Different water flow conditions and vegetation characteristics (mainly the number) are varied to change the drag force. The drag coefficient C_d along the water depth within the vegetation layer is analyzed under three different working scenarios summarized in Table 1. The C_d is closely related to the number of plants per unit area, and the frontal area that blocks the flow. In ecological studies, these quantities are combined and expressed as the plant density a, which is the positive

Table 1 Experimental parameters for the three cases discussed in this paper

Case	n / m^{-2}	b / m	S /%	l /m	H /m	U_m/m·s^{-1}	h_v /m
1	43.3	0.15	0.01	0.15	0.27	0.12	0.185
2	108.3	0.10	0.04	0.10	0.27	0.13	0.195
3	108.3	0.10	0.04	0.10	0.33	0.11	0.210

area blocked by the vegetation per unit volume[78]. In the experiments here, the number of plants considered varied by the conditions listed in Table 1 and are $n_1 = 43.3 \text{ plants} / \text{m}^2$ and $n_2 = 108.3 \text{ plants} / \text{m}^2$. The water blocking area on the front of the vegetation cannot be directly calculated because of the irregular vertical distribution of the plastic water weed area.

Fig. 4 Illustration of the projected area of a vegetation element used to compute the frontal area A_f (black color)

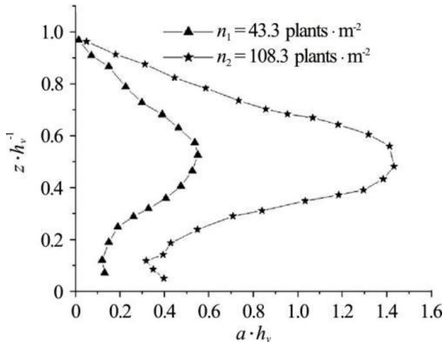

Fig. 5 Variation of vegetation density along the vertical direction, where triangles indicate $n_1 = 43.3 \text{ plants} / \text{m}^2$, and star indicates plant number $n_2 = 108.3 \text{ plants} / \text{m}^2$.

A MATLAB image processing software is used for the calculation of the projected frontal area A_f derived for a single vegetation element (shown in Fig. 4), and the plant area density is then expressed as

$$a(z) = \frac{nA_f(z)}{\Delta z} \tag{1}$$

where $\Delta z = 0.01$ m . The computed vertical distribution of the plant density is far from uniform as shown in Fig. 5. The plant density first increases from the channel bottom to $z / h_v = 0.5$ and then decreases to the vegetation top. The plant density increases with n unlike the experiments conducted by Nepf and Vivoni[65]. In their experiment, the plant density remains constant first, increases in the interval $0.1 < z / h_v < 0.5$, and reaches a maximum value when $z / h_v > 0.5$. The reason for the increase of the plant density in the experiment here is that the leaves are narrow-on-side and wide-in-the middle. By contrast, the vegetation model by Nepf and Vivoni[65] is composed of six rectangular narrow plastic sheets with regular shapes. Thus, the trends of vegetation density between the experiment here and the Nepf-Vivoni experiment are different.

The effective drag coefficient of the vegetation $C_d(z)$ can be obtained based on the mean momentum equation of the vegetated flow for completely developed stage ($x / L_v > 0.58$, see Section 2.2) [29]

$$\frac{\partial(-\overline{u'w'})}{\partial z} + gS - \frac{1}{2} C_d a U^2 = 0 \tag{2}$$

where the viscous stresses and the bottom roughness are ignored. The measured relation between C_d and z / h_v is shown in Fig. 6. An empirical expression can be fitted to the measurements based on a parabolic shape and is given as

$$C_d = 8\left(\frac{z}{h_v} - \frac{1}{2}\right)^2 + \frac{1}{3} \tag{3}$$

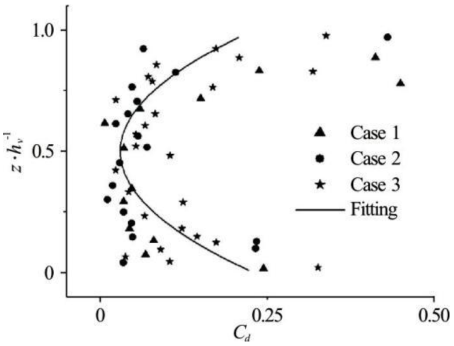

Fig. 6 Relation between measured C_d and z / h_v in all three cases for a completely developed stage ($x / L_v > 0.58$).

From Figs. 5, 6, it can be seen that the profile of the frontal width influences the computed vegetation drag. Near the center of the vegetation stem, the frontal area reaches its maximum value whereas the vegetation drag reaches its minimum. This finding differs from the cases of a flow through rigid vegetation with a uniform frontal width. In future models, it becomes necessary to consider variations in the drag coefficient for various shapes of a vegetation array along the vertical direction.

2.2 Flow in the streamwise direction

Figure 7 shows the mean velocity profile as a function of z / h_v in a typical cross-section (approximately $x / L_v = 0.58$) for all three experimental conditions. As shown in Fig. 7, the mean velocity profile assumes an "S" shape with an inflection point below the top of the vegetation layer. The mean velocity gradient reaches a maximum value at approximately $z / h_v = 0.6$ corresponding to the location of the maximum mean vorticity. Within the vegetation layer $(z / h_v < 1)$, the dimensionless velocity profiles in all three cases are similar.

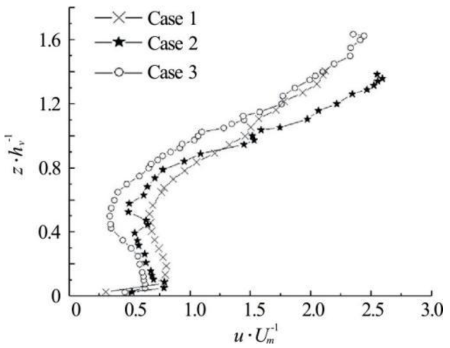

Fig. 7 Variation of the mean longitudinal velocity profile at $x / L_v = 0.58$ for the three cases highlighted in Table 1. Note the approximate S shape in all 3 cases.

Hence, on the basis of these measurements and the similarity in the shapes of the mean velocity profiles in all 3 cases, we have identified three subzones from the bottom to the top: (1). The vegetation layer $(0 < z / h_v < 0.6)$ in which the mean velocity profile assumes roughly an "S" shape. The S shape is the result of the interplay between the drag force, the gravitational potential, and the momentum flux gradient due to the vegetation. In the lower part $(0 < z / h_v < 0.2)$, the leaf area density is sufficiently small that the mean velocity is shaped by the gravitational potential and the mean momentum flux. This balance results in a mean velocity profile that increases with z. In the middle part $(0.2 < z / h_v < 0.6)$, the leaf area is near its maximum. Here, the drag force causes an appreciable slow-down of the mean velocity in this zone. (2). Above the vegetation zone $(z / h_v > 1)$, the drag force is entirely absent, the magnitude of the shear stress declines and approaches zero at the free water surface causing the mean velocity to rapidly increase with z. (3) Near the top of the vegetation layer $(0.6 < z / h_v < 1.2)$, where one sees the velocity difference at the interface between the vegetation layer and the non-vegetation layer, a shear layer forms. As shown in Fig. 7, the mean velocity above the top of the vegetation layer varies approximately logarithmically. The existence of the vegetation alters the Reynolds stress, and the turbulence intensity profiles as expected. The turbulence intensity is conventionally defined as the root mean squared deviation value of a turbulent velocity component, that is, $U_{irms} = \sqrt{u_i'^2}$. The mean velocity, the Reynolds stress, and the turbulence intensity profiles are shown in Fig. 8.

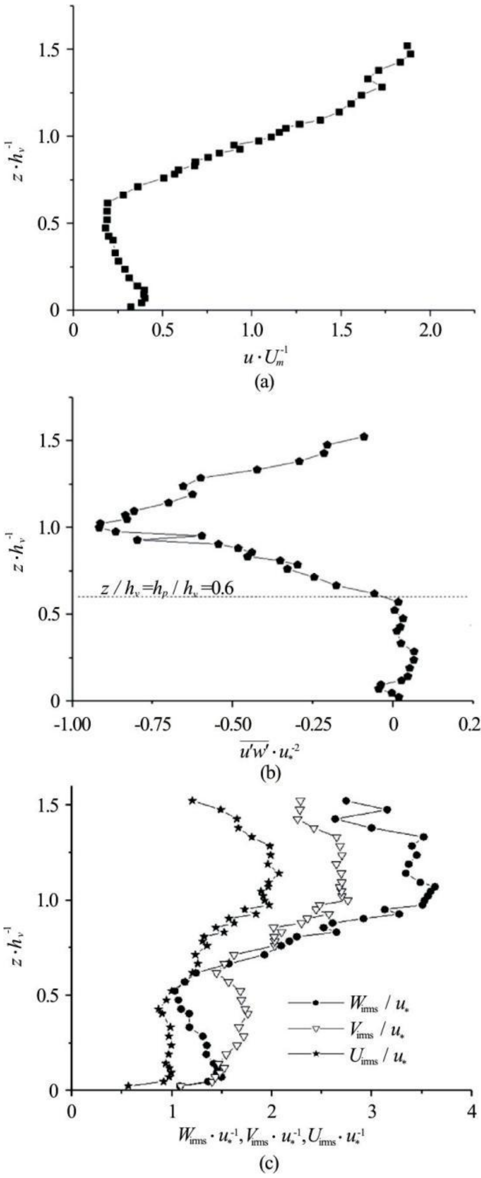

Fig. 8 Vertical variation of the mean velocity (a), the Reynolds stress (b), and the turbulence intensity (c) at $x / L_v = 0.58$ in case 1

Compared to the mean momentum flux- and mean velocity profiles, the turbulent intensities do not vary as appreciably and the attenuation of these flow statistics remains modest. The strong momentum

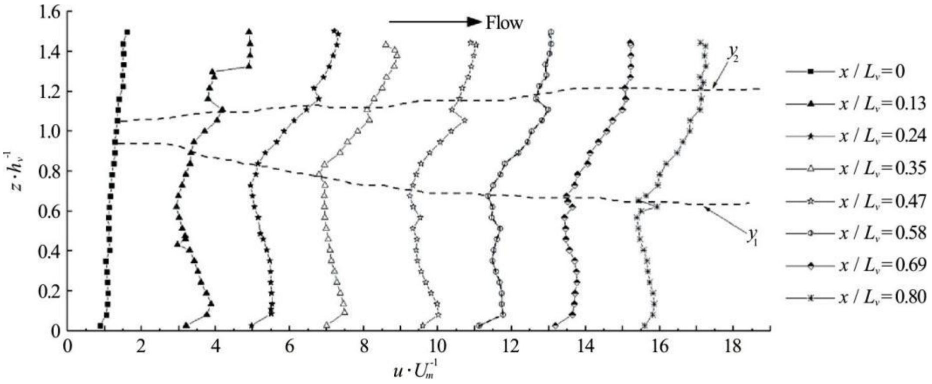

Fig. 9 Development of the mean longitudinal velocity at various cross-sections in case 1. The thickness of the mixing layer is denoted by dashed lines, y_1, y_2 .

vertical exchange near the top of the vegetation layer causes the turbulent shear stress to "invade" into the vegetation layer. The depth where the turbulent shear stress within the vegetation layer decreases to some 10% of the maximum shear stress value is defined as the intrusion depth h_p [65], as shown in Fig. 8. The Reynolds stress reaches its maximum at the interface between the vegetation layer and the non-vegetation layer, indicating the existence of a strong shear effect, and gradually decreases toward the water surface (approximately linearly, as consistent with Eq. (2)) and the bottom of the channel (due to the momentum absorption by the vegetation). Inside the vegetation, the Reynolds stress approaches zero below the intrusion depth $z/h_v = h_p/h_v = 0.6$. In this layer, the gravitational force is only balanced by the vegetation drag force, thereby dictating the value of the mean velocity in this zone (as earlier discussed).

For the turbulence intensity, the longitudinal, lateral, and vertical turbulence intensities reach their maximum values at the interface between the vegetation layer and the non-vegetation layer and decrease toward the water surface and the bottom of the channel. An interesting feature is that the flow is energetically more "isotropic" inside the vegetation as compared to the vegetation free zone. That is, the presence of the vegetation seems to enhance the return-to-isotropy through the generation of fine-scale wakes.

After the discussion of the profile shapes of the first and second moments of the flow, we now turn our attention to the longitudinal development of the mean velocity profile. Starting from an approximately well-mixed mean velocity profile prior to encountering the vegetation section, the longitudinal distance to attain an equilibrium zone with the vegetation can be determined. Beyond this distance, the profile shapes of the flow statistics become nearly independent of x . The first feature to note during this equilibrium phase is a stable vortex structure, which is slowly being produced when the water flows through the vegetation section (as shown in Fig. 9). The downstream distance and the longitudinal velocity are normalized by the length of the vegetation model patch L_v and the cross-sectional velocity U_m . The mixing layer is shown as the region between two inflection points (y_1, y_2) of the time-averaged velocity along the downstream direction. As shown in Fig. 9, the adjustment process is divided into three stages:

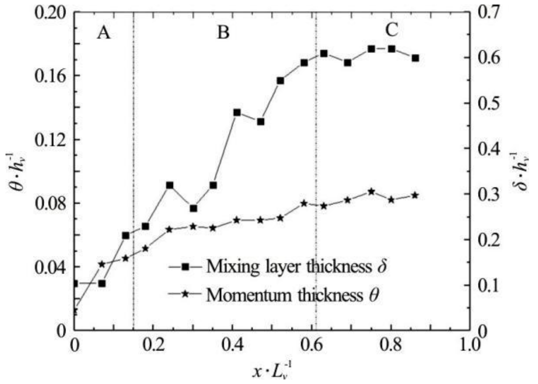

Fig. 10 Growth of the mixing layer and the momentum thickness downstream along the edge of the vegetation model patch in case 1, where A denotes diverging flow stage, B denotes development stage, and C denotes completely developed stage

(1) The first stage is the diverging flow stage. The pressure in the front part of the vegetation increases due to the presence of the vegetation, and the velocity in the vegetation layer continues to decrease. A strong outward flux occurs at the top of the vegetation layer due to the drag force within the vegetation. The shear layer is not formed in this stage yet, and the turbulent stress remains weak and can be neglected.

(2) The second stage is the development stage, in which the mixing layer at the top of the vegetation layer gradually develops, and the shear stress starts to increase and reaches an equilibrium.

(3) The third stage is a completely developed stage, where the mixing layer is now developed and its growth is almost independent of the longitudinal distance. The layers above the mixing layer are adjusted based on the boundary conditions and are also equilibrated with the presence of the vegetation. The downstream velocity is roughly unchanged

$(\partial U / \partial x \approx 0)$ beyond this point. On the basis of the

adjustment flow process, the flow region is reasonably approximated by three longitudinal sub-zones, namely, the diverging flow, the development, and the completely developed zones.

Figure 10 presents the longitudinal development of the mixing layer depth and the momentum thickness, which gradually increase and then stabilize (i.e., become independent of x). The momentum thickness can be calculated as

$$\theta = \int_0^\infty \left[\frac{1}{4}\left(\frac{U - \bar{U}}{\Delta U}\right)\right] dz \qquad (4)$$

where ΔU is a velocity difference and can be obtained from $\Delta U = U_2 - U_1$, U_1 , U_2 are low- and high-stream velocities, and $\bar{U}$ is defined as their mean $\bar{U} = (U_1 + U_2) / 2$. As shown in Fig. 10, the mixing layer and momentum thicknesses stabilize at approximately $x / L_v = 0.52$ from the leading edge of the vegetation model patch (recall that the prior analysis of the mean velocity and the turbulent stress is conducted at $x / L_v = 0.58$). The stabilization distance of the mixing layer thickness is also consistent with prior experiments by Ghisalberti and Nepf[79]. It is expected that the development of the mixing layer thickness be confined by the boundary conditions, namely, the water depth and the channel bottom. It is to be noted that a canonical mixing layer thickness continually develops down- stream in an unobstructed shear layer. The ratio of the mixing layer thickness δ to the momentum thickness θ is approximately 7.5, which agrees with the result of Nezu and Sanjou[80], giving $\delta / \theta \approx (7\text{-}8)$.

The development of the mixing layer and the momentum thickness along the longitudinal distance has practical engineering significance when determining distances of the adjustment zones from the vegetation inlet to the equilibrium zone. This longitudinal distance is hereafter labeled as X_D . The which is consistent with the experimental results of Rominger and Nepf [81]. They proposed that the length scale X_D in the low flow-blockage cases ($\overline{C_d}\bar{a}h_v < 2$, where h_v = 0.185 m is the height of the vegetation patch in the vertical direction, $\bar{a}$ is the depth-averaged vegetation density, and $\overline{C_d}$ is the depth-averaged drag coefficient) is given by

$$X_D = (3 \pm 0.3)\left\{\frac{2}{\overline{C_d a}}\left[1 + (\overline{C_d}\bar{a}B_v)^2\right]\right\} \qquad (5)$$

Based on this expression, the calculated $X_D \approx 3.9$ m is in line with the independently measured length scale here. Hence, the vegetated flow can be assumed to be completely developed at distances greater than $X_D / L_v = 0.52$ from the leading edge of the vegetation patch.

2.3 Mechanics of turbulent structure in vegetated flow

The energy spectra and quadrant analysis

methods are commonly used to analyze turbulent flow structures. These two methods are used to quantify size, energetics, and momentum transporting events.

measured length scale X_D is about 4.1 m here,

2.3.1 Power spectral density

As earlier noted, the K-H instability occurs near the canopy top and is responsible for the attainment of the mixing layer. The scale of the shear layer gradually increases with the downstream distance and remains constant until the dissipation term of the turbulent kinetic energy of the flow is balanced by the mechanical and wake production generation terms. A coherent vortex structure can be identified by the periodic oscillation in the longitudinal and vertical velocity component time series. Figure 11 shows the time series of the longitudinal and vertical velocities at the interface between the vegetated and non-vegetated layers at a representative cross-section (near $x / L_v = 0.58$) in the three different cases of Table 1. The fluctuations of the longitudinal and vertical velocities are anti-correlated, which indicate a strong vertical momentum exchange. The oscillation frequency of the longitudinal velocity is the same as that of the vortex propagation. The frequency of the momentum transport oscillation is twice the vortex frequency. As mentioned above, the vegetation layer creates a coherent vortex, which induces periodic fluctuations of the velocity at the top of the vegetation layer and dominates the vertical momentum transport (as seen inFig. 11).

in resonance, which are consistent with the frequency of the vortex diffusion. To determine the frequency of the vortex diffusion, a spectral analysis is conducted to analyze the vertical fluctuation velocity w' at the top of the vegetation layer.

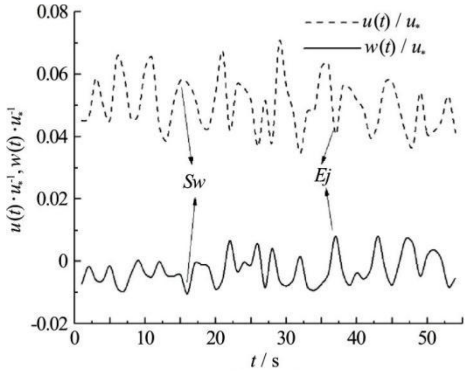

(a) Case 1

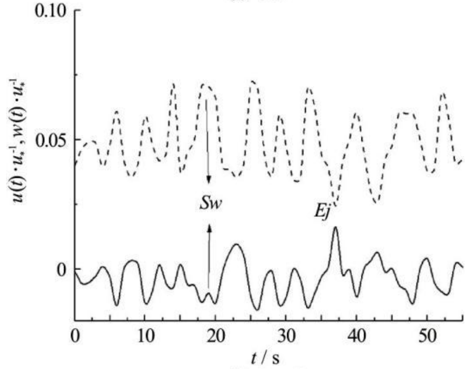

(b) Case 2

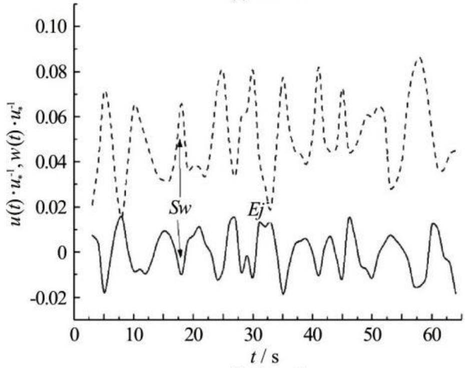

(c) Case 3

Fig. 11 Time series of longitudinal velocity and Reynolds stress versus time at a completely developed cross-section in all three cases ($x/L_v = 0.58$, $y/B = 0.5$ and $z/h_v = 1$). Strong Reynold stresses are marked as ejection (Ej) and sweep (Sw). Details about the two flow types are discussed in Section 2.3.2)

The energy spectrum of the vertical velocity fluctuations at the top of the vegetation layer is computed and shown in Fig. 12. The energy spectrum can be divided into three sub-regions: the large-scale coherent vortex sub-region, the shear production sub-region, and the inertial sub-region. The vortex structure in the large-scale region appears as a "bump" in the vertical turbulent kinetic energy component. For the inertial sub-region, the energy spectrum approximately satisfies the Kolmogorov turbulence spectrum with a –5/3 power law scaling at high frequencies. In this sub-region, the viscous dissipation of the flow can be ignored. Most turbulent kinetic energy dissipation occurs in the high-frequency range, which cannot be resolved by the ADV. In fact, an approximate instrument white-noise flat spectrum appears to dominate the frequencies beyond 20 Hz demonstrating the sampling limits of the experiment.

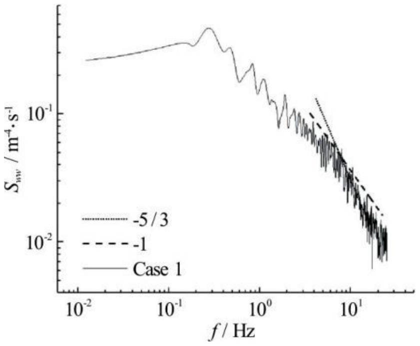

Fig. 12 Power spectral density of vertical velocity sampled at the top of the vegetation layer and at a representative location $(x/L_v = 0.58)$ in case 1. The exponent of the line associated with the locally homogeneous and isotropic turbulence predicted from Kolmogorov's theory is –5/3. The –1 power-law is shown for reference

An approximate f^{-1} power-law scaling emerges followed by an approximate −5/3 with increasing frequency. Typically, a –1 power-law scaling in the spectrum (either in f or the wavenumber k) suggests that the spectrum in this range of eddy sizes becomes independent of the length scale that produces the energy $(= L_E)$, Here, L_E may be regarded as the momentum thickness (see Fig. 12(a)) or the stem diameter (see Fig. 12(b)) depending on y/b. The following dimensional assumptions may be adopted to discuss the plausibility of the occurrence of a –1 power-law at scales smaller than L_E. Considering that the velocity variances are ultimately produced by the gravitational force that drives the flow (i.e., $u_{*,b}^2$), the dimensionless energy spectrum at the large and intermediate ranges of scales relevant to the energy production (i.e., where the majority of variance lies) may be normalized as[82-83]

$$\frac{S_{ww}(k)}{u_{*,b}^2 L_E} = F_s(kL_E) \tag{6}$$

where k is a wavenumber, and $F_s(kL_E)$ is a similarity function to be determined as a function of the dimensionless wavenumber (kL_E) . The only means to cancel L_E from the two sides of this expression is by setting $F_s(kL_E) = A_E/(kL_E)$ thereby producing a −1 power-law scaling when the spectrum of eddies with sizes smaller than L_E becomes independent of L_E (they have not completely attained their near-isotropic state given by Kolmogorov's −5/3 scaling with increasing f), where A_E is a similarity constant that may vary with H . Specifically, the −1 power-law scaling is expected to occur at eddy sizes smaller than L_E but larger than eddy sizes associated with Kolmogorov inertial regime. The range of scales that are described by a near −1 power-law scaling in Fig. 12 appears consistent with the aforementioned analysis. However, this analysis should be further investigated using LES and laser-Doppler anemometry measurements.

The periodicity of oscillations in the longitudinal and vertical velocities means the existence of a single dominant frequency component, which we now seek to explore longitudinally. The spectrum of the vertical velocity fluctuations at the top of the vegetation layer is now computed at various longitudinal positions and the calculated frequency is normalized by the momen- tum thickness and the spatially-averaged velocity, as shown in Fig. 13. The peak in the energy spectrum curve allows the determination of the frequency of the coherent vortex structure in the mixing layer. As shown in Fig. 13, the dominant frequency of the vortex remains basically unchanged during its development along the flow direction. The peak of the energy spectrum curve is mainly concentrated at $f\theta/\bar{U} = 0.027$ when the water depth is the same but the vegetation density is different (as shown in Figs. 13(a), 13(b)), However the peak of the energy spectrum curve becomes concentrated at $f\theta/\bar{U} = 0.04$ with increase in water depth. This is because the momentum thickness θ increases with the increase in water depth, and so will $f\theta/\bar{U}$. Compared with the rigid vegetation, the dimensionless frequency $f\theta/\bar{U}$ is constantly maintained at 0.032 regardless of the experimental parameters such as water depth and vegetation density [84], whereas the dimensionless frequency $f\theta/\bar{U}$ of the flexible vegetation model changes with water flow. This may be attributed to the rigid vegetation not swaying with the flow, whereas the flexible vegetation here is irregular in shape and swings randomly.

2.3.2 Momentum transfer and quadrant analysis

The quadrant analysis is used for analyzing the turbulent structures that contribute to the momentum transport. Lu and Willmarth[85] first adopted this method when investigating the shear stress characteristics at the boundary layer outside the turbulent viscous layer. The basic principle of quadrant analysis is decomposing the Reynolds stress into four flow types labeled as Q_1 , Q_2 , Q_3 and Q_4 in the u' - w' plane based on the signs of the longitudinal velocity fluctuation u' and the vertical velocity fluctuation w' (as shown in Fig. 14). At a given point, these quadrants correspond to Q_1 being the outward interaction ($u' > 0$, $w' > 0$), which is the upward movement of the high-speed fluid , Q_2 being an ejection event ($u' < 0$, $w' > 0$), which is the upward movement of the low-speed fluid, Q_3 is the inward interaction ($u' < 0$, $w' < 0$), which is the downward movement of low-speed fluid, and Q_4 being the sweeping event ($u' > 0$, $w' < 0$), which is the downward movement of the high-speed fluid .

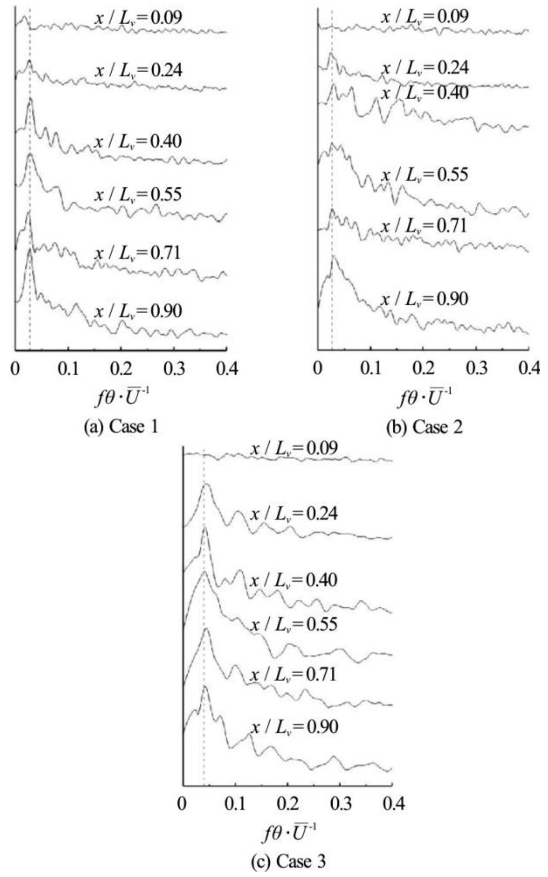

(a) Case 1

(b) Case 2

(c) Case 3

Fig. 13 Non-dimensionalized energy spectra at various x - positions from the leading edge of the vegetated patch for the three different cases listed in Table 1.

Figure 14 presents a sketch of the four quadrants responsible for the momentum exchange at a given point along with the so-called hyperbolic hole. The four quadrants are separated by a “hole” defined by $|u'w'| = H_0|\overline{u'w'}|$, where H_0 is the threshold value that represents the “hole” size. The importance of establishing a “hole” domain is that large values of the Reynolds stress in each quadrant can be extracted with the back-ground small events removed.

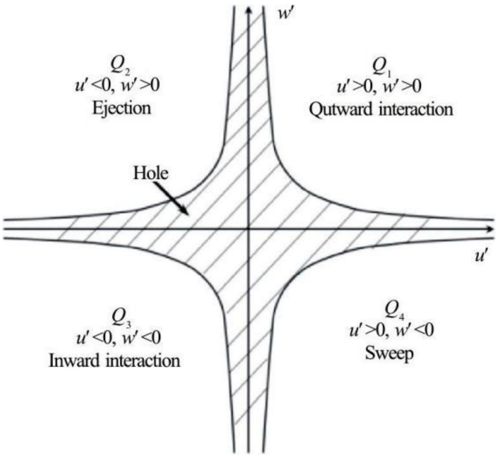

Fig. 14 Schematic diagram of the quadrants and the "hole" region

The contribution of each flow type to the local Reynolds stress is calculated as:

$$S_{i,H_0} = \frac{1}{T}\int_0^T C_{i,H_0}(t)u'(t)w'(t)\ \mathrm{d}t \qquad (7)$$

$$C_{i,H_0} = 1,\quad |u'(t)w'(t)| > H_0|\overline{u'w'}| \quad \text{and} \quad [w'(t), w'(t)]$$

in the quadrant Q_i (8a)

$$C_{i,H_0} = 0 \quad \text{otherwise} \qquad (8b)$$

where T is the measurement duration, C_{i,H_0} is the average condition, and u' and w' are the longitudinal and vertical fluctuation velocities at the measurement point, respectively. Contribution values S_{i,H_0} are normalized by the Reynolds stress so that

$$\hat{S}_{i,H_0} = \frac{1}{Tu_*^2}\int_0^T C_{i,H_0}(t)u'(t)w'(t)\ \mathrm{d}t$$

and

$$\sum_{i=1}^{4}\hat{S}_{i,0} = -1 \quad \text{when} \quad H_0 = 0 \qquad (9)$$

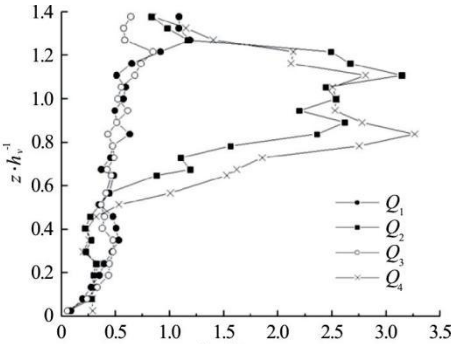

(a) Case 1

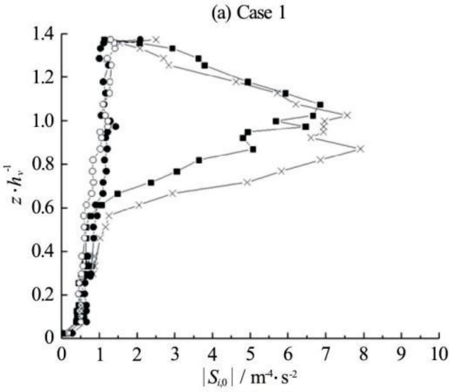

(b) Case 2

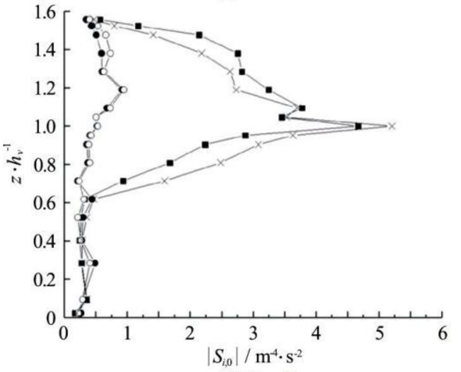

(c) Case 3

Fig. 15 Contributions of each quadrant to the Reynolds stress for the three cases listed in Table 1.

Figure 15 shows the vertical distribution of the absolute contribution values for various water depths and vegetation densities in the completely developed zone (i.e., $x/L_{\text{veg}} = 0.58$). As shown in this figure, the Reynolds stress in the vicinity of the top of the vegetation layer $(z/h_v \approx 1)$ is dominated by both ejections and sweeps. The contribution of ejections and sweeps to the Reynolds stress reaches a maximum at the top of the canopy and decreases toward the free water surface and the channel bed. The contribution of ejections to the Reynolds stress above the top of the vegetation layer $(z/h_v > 1)$ is greater than that of the sweeps, and the ejection is the dominant flow type in this zone. Meanwhile, the situation below the top of the vegetation layer ($0.6 < z / h_v < 1$) is opposite and sweeps are dominant. The comparison of the results for the three cases in Table 1 shows that the peak in case 3 is sharper than the peaks in cases 1, 2. This finding is because the vegetation does not show a *monami* (or waving) phenomenon in case 3, and the vegetation maintains an upright state similar to rigid vegetation. In this case, the flow structure is similar to the rigid-vegetated flow, where the ejection-sweep transition near the peak is rapid[86]. In cases 1, 2, the vegetation sways with the flow and the swing of the blade enhances the vertical transfer of turbulent kinetic energy.

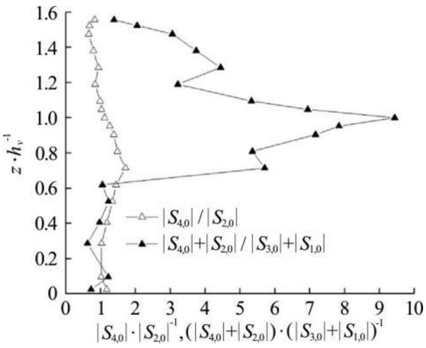

Fig. 16 Ratio of contributions of various quadrants to momentum transfer at a representative cross-section in case 3

Figure 16 illustrates the ratios of the inward and outward interactions to sweeps and ejections $(|S_{2,0}|+|S_{4,0}|)/(|S_{1,0}|+|S_{3,0}|)$ and the ratios of the sweep to the ejection $|S_{4,0}|/|S_{2,0}|$ at the representative cross-section $(x / L_v = 0.58)$ in case 3. As shown in Fig. 16, the contributions of ejections and sweeps are equivalent to those of the inward and outward interactions below $z / h_v = 0.6$. The contributions of ejections and sweeps are prominent when $z / h_v > 0.6$, especially at the top of the vegetation layer, and gradually decrease towards the water surface and the bottom of the channel. For the ratio of ejections to sweeps, sweeps dominate inside the vegetation layer, whereas ejection dominates inside the non-vegetation layer. The sweep strength is remarkably greater than that of its ejection counterpart. These findings indicate that sweeps and ejections are dominant, and sweeps are stronger than ejections in the vicinity of the top of the vegetation layer (i.e., in the mixing layer). These results are similar to the findings reported for rigid rods and canopies with complex morphologies such as forests[32, 87- 88].

The development of $(|S_{2,H_0}|+|S_{4,H_0}|)/(|S_{1,H_0}|+|S_{3,H_0}|)$ is different for varying threshold values of H_0 . Figure 17 presents the profile ratio of inward and outward interactions to sweeps and ejections for different threshold values ranging from 0 to 6. The contributions of ejections and sweeps inside the vegetation layer and near the water surface are basically equivalent to the contribution of inward and outward interactions (where the mean momentum flux is almost zero). The contributions of ejections and sweeps to the Reynolds stress in the vicinity of the top of the vegetation layer is remarkably greater than those of the inward and outward interactions. The ratio $(|S_{2,H_0}|+|S_{4,H_0}|)/(|S_{1,H_0}|+|S_{3,H_0}|)$ gradually grows with increasing H_0, which indicates that ejections and sweeps contribute more to the Reynolds stress. The hole region eliminates more large values of the Reynolds stress in each quadrant with increasing hole size. The contribution of ejections and sweeps to Reynolds stresses is greater than that of inward and outward interactions when the threshold $H_0 = 0$ near the top of the vegetation layer. Hence, the elimination of large events from each quadrant makes the sum of ejections and sweeps larger than that of inward and outward interactions.

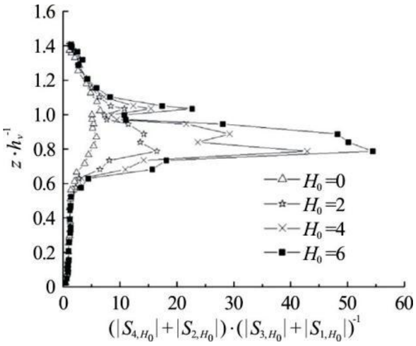

Fig. 17 The ratio $(|S_{2,H_0}|+|S_{4,H_0}|)/(|S_{1,H_0}|+|S_{3,H_0}|)$ for increasing thresholds H_0 in case 3.

The sum of ejections and sweeps contributions at the top of the vegetation layer for different threshold values (H_0 = 0 - 8) is normalized, as shown below

$$S^*(H_0) = \frac{S_{2,H_0} + S_{4,H_0}}{S_{2,0} + S_{4,0}} \tag{10}$$

and we define $T^*(H_0)$ as

$$T^*(H_0) = \frac{1}{T}\int_0^T [C_{2,H_0}(t) + C_{4,H_0}(t)]\mathrm{d}t \,. \tag{11}$$

A relation between $S^*(H_0)$ and $T^*(H_0)$ can be obtained and is shown in Fig. 18. Here, S^* indicates the proportion of total contribution of ejections and sweeps occupied by large values. However, T^* measures the ratio of times taken to generate ejections and sweeps normalized by the total sampling time. As shown in Fig. 18, 80% of ejections and sweeps occur within 30% of the recording time. This short duration and large momentum transport contribution is suggestive that ejections and sweeps are caused by large coherent vortex motion. This finding is consistent with the conclusion of Ghisalberti and Nepf[86] and many others as reviewed elsewhere[32].

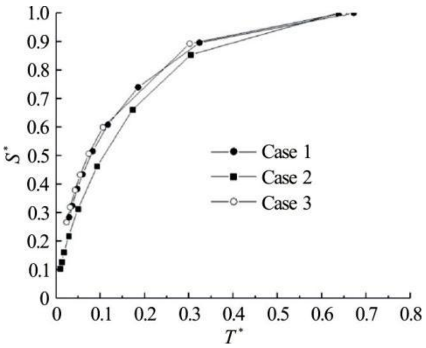

Fig. 18 Relation between the ratio of ejections and sweeps to fractional time for the three different cases in Table 1.

From the above quadrant analysis, it can be concluded that the flow pattern at the top of the vegetation layer is mainly characterized by ejections and sweeps, and sweeping effects are stronger than that of ejections. This phenomenon may be analyzed from the perspective of mean longitudinal velocity U, the Reynolds stress $u'w'$, and the vertical distribution of the turbulence intensity w_{irms}. The mean velocity distribution is in an “S” shape, as shown in Fig. 19. Two adjacent layers, namely, a and b, are used at the top of the vegetation layer for illustration. The vertical velocity fluctuations $(w' > 0)$ are observed when a unit volume of a water body moves to the upper layer. Meanwhile, the water body in the lower layer entering the upper layer will reduce the upper flow velocity (relative to the mean) because the longitudinal velocity gradually increases toward the water surface. Hence, the longitudinal fluctuation velocity $u' < 0$ is observed. An ejection event in the second quadrant ($u' < 0$, $w' > 0$) is the outcome of such a motion. Similarly, when the vertical fluctuation velocity $w' < 0$ is observed, $u' > 0$. At this instant, the flow type corresponds to a sweeping event contributing to the fourth quadrant ($u' > 0$, $w' < 0$). To summarize, the two main flow types at the interface of the vegetation layer and the non-vegetation layer are ejections and sweeps as expected with sweeps more dominant in the vegetation layer and ejections more dominant in the vegetation free layer simply due to the turbulent intensities.

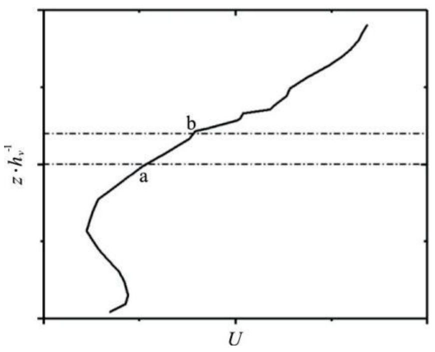

Fig. 19 Profile of the mean longitudinal velocity along the water depth direction as well as two points illustrating the expected contribution to the Reynolds stress of sweeps and ejections when the vertical velocity fluctuations are symmetric.

3. Conclusions

The main results and conclusions are as follows:

(1) The dimensionless vegetation drag coefficient profile assumes an approximate parabolic shape with a decreasing trend in the range $0 < z / h_v < 0.5$ and an increasing trend in the range $0.5 < z / h_v < 1$. The height at which the drag coefficient is most reduced coincides with the location of maximum leaf area and is suggestive of an enhanced sheltering at this location. For future studies of the mean velocity profile, it is necessary to consider the interplay between the vegetation density, the foliage type, and drag reductions vertically.

(2) The presence of vegetation causes a discontinuous resistance in the vertical direction, and in turn a vertical variation in the mean longitudinal velocity with an inflection point (fast above, slow inside the vegetation). Hence, a coherent vortex structure is produced at the top of the vegetation layer, as is consistent with numerous canopy flows (aquatic and terrestrial alike). On the basis of the measured mean velocity in equilibrium with the vegetation section, the water flow can be divided into three distinct zones: inside the vegetation layer, near the top of the vegetation layer, and above the vegetation layer. In the vegetation layer, the velocity distribution is “S” shaped and the mean velocity gradient is negative. The mean velocity near the top of the vegetation layer varies approximately logarithmically. In the upper part of the vegetation layer, the water flow is similar to a canonical open channel flow, and the vertical variation of the mean longitudinal velocity is similar to a “J” shape. The Reynolds stress and the turbulent

intensity reach their maximum at the interface of the vegetation and non-vegetation layers and gradually decrease towards the water surface and the bottom of the channel as expected. The turbulent intensities within the vegetation layer decrease, whereas the velocity in the non-vegetation layer increases with the increase in height. The longitudinal development of the momentum thickness is consistent with that of the thickness of a canonical mixing layer.

(3) The main flow type near the top of the vegetation layer is ejections and the sweeps, and the intensity of sweeps is greater than that of ejections, again consistent with numerous studies of flow through vegetation. Each strong sweep is accompanied by a weak ejection. The power spectral density for vertical velocity fluctuations at the top of the vegetation layer satisfies the Kolmogorov turbulent kinetic energy spectrum with a $-5/3$ power law at high (resolved) frequencies. New sets of power spectral density curves are obtained after the frequency of the energy spectrum curve is normalized by the spatial-averaged velocity $\bar{U}$ and the momentum thickness θ of the mixing layer. From the power spectral analysis, the peaks of the dimensionless power spectral density curves are concentrated at 0.027 for different flexible vegetation densities but for the same water depth. The peaks are located at 0.04 for the same density but different water depths. The findings here show that the variations of the dimensionless power spectral density curves are closely related with the flow depth instead of the vegetation density. However, the dominant frequency for the rigid vegetated-flow remains unchanged under different experimental conditions. This shift is because the shape of the flexible vegetation model tends to randomly swing with the flow.

(4) The ejections and the sweeps are dominant at the top of the vegetation layer, and the sweep events are stronger than the ejection events inside the canopy. Ejections and sweeps are both short and intense. Approximately 80% of ejections and sweeps are completed within 30% of the sampling time near the canopy top (i.e., the location of the maximum turbulent stress). These results are in agreement with numerous canopy flow experiments, including forested canopies.

4. Future work

Future model developments that accommodate the aforementioned findings, especially regarding the role of ejections and sweeps, are aimed at new closure schemes for momentum flux transport terms (i.e., the triple moments). In particular, relations between quadrant analysis, momentum flux transport, and cumulant expansion of the joint probability density function of w' , u' pave the way for the so-called structural turbulence closure schemes. These schemes can take full advantage of the experiments reported here and offer a different perspective than gradient-diffusion closure. A summary of several future directions are now outlined.

4.1 Numerical simulation of vegetated flow

4.2 Numerical simulation is a power tool to investigate the flow structure under different situations[89-90]. In our previous work, an LES model was established to explore local blockage of artificial vegetation patches in rectangular open channels partially covered by a rigid cylindrical vegetation array[25], where the influence of turbulent structures on momentum transfer along the vegetation periphery was studied. Results show that the LES agree well with the experimental results lending confidence inthe LES model for vegetated flow. Lu and Dai[91-93] adopted an LES model with flexible vegetation, wherethe deflected height of flexible vegetation was considered in the model and a Runge-Kutta scheme was combined with the operator splitting algorithm to solve the governing equations. Scalar transport was also simulated using Eulerian and Lagrangian models. Results showed that the vertical mixing and the diffusion of scalar concentration can be enhanced by flexible vegetation. The model can quantitatively predict the decreasing trend of concentration distribution along the flow direction with increase in vegetation density.

4.3 Interaction between vegetation, pollutant transport and sediments in flow

To represent the impact of vegetation in wetlands on pollutant transport, previous LES work focused on vertical buoyancy jet injecting cross-flow for rigid vegetation. The existence of vegetation elements reduce the velocity of the channel, thus significantly increasing the penetration height and the dilution of the jet. The vortex lengths corresponding to the dominant frequencies at different positions in the flow can be studied by means of spectral analysis. From another perspective, the vegetation in wetland, open channel or lakes affects the longitudinal dispersion, the lateral diffusion and the velocity distribution, thus the flow region can be divided into several layers/zones according to the characteristics of the turbulent structure.

Future investigations of sediments will use the random displacement model (RDM)[94] that offers a powerful tool to simulate particle transport in vegetated flows. Concentrations are represented by a large number of independent particles to model material transport in the flow. Compared to the Eulerian method (EM) that focuses on concentration at the whole region, the RDM in the Lagrangian mode has several advantages[95]. Firstly, with RDM, the motion and the position of particles are directly displayed, while with the EM, only the positions with crowded particles are shown. Secondly, the scale of the source in the EM is always much smaller than the spatial resolution, which makes the representation of the source difficult, but the RDM does not have such shortcomings. Thirdly, the RDM has a high computational efficiency by focusing on the region with more particles. Last but not least, with the RDM, we do not have the artificial dispersion because the steep concentration gradient has no effect on the RDM. We plan to conduct new flume experiments where particles are introduced and their dispersion/capture by vegetation analyzed to test RDM and EM predictions.

4.4 Application for ecological environment reconstruction

Ecological environment reconstruction, also called phytoremediation, can be applied based on the theory of hydrodynamics for flow through vegetation. As previously noted, phytoremediation refers to the adoption of vegetation/plants with coexisting microbial systems to remove pollutants and restore ecological function. It is shown that pollutants in soil or water can be purified by means of absorption, volatilization, root filtration, degradation and stabilization of vegetation. The function of vegetation in ecological reconstruction can be summarized as follows: (1) purification by absorption and enrichment of aquatic vegetation, (2) sedimentation and filtration of aquatic plants, and (3) inhibition of aquatic plants on algae.

Future flume experiments aimed at developing theories for phytoremediation will focus on: (1) optimal plant morphology and density to be used in ecological restoration, (2) the effects of combining different aquatic plants and their optimal configuration for pollutant purification based on merging hydrodynamics and biochemistry of vegetated flow, (3) harvesting and subsequent treatment of aquatic plants to avoid secondary pollution. These planned flume experiments will assist in ecological restoration of moving water bodies,

where plants play a key role.

References

[1] Richardson D., Holmes P., Esler K. et al. Riparian vegetation: Degradation, alien plant invasions, and restoration prospects [J]. *Diversity and Distributions*, 2010, 13(1):126-139.

[2] Huang W., Yano S., Lin L. et al. Using functional indicators to assess the river health under partial flow restoration [C]. *International Symposium on Water Resource and Environmental Protection*, Xi'an, China, 2011.

[3] Sun Z., Chang N. B., Opp C. et al. Evaluation of ecological restoration through vegetation patterns in the lower Tarim River, China with MODIS NDVI data [J]. *Ecological Informatics*, 2011, 6(2): 156-163.

[4] Dong Z. R. Scale and pattern for ecological restoration of river [J]. *Journal of Hydraulic Engineering*, 2006, 37(12): 1476-1481 (in Chinese).

[5] Zhang H. B., Meng H. J., Liu X. D. et al. Vegetation characteristics and ecological restoration technology of typical degradation wetlands in the middle of Heihe River Basin, Zhangye City of Gansu Province [J]. *Wetland Science*, 2012, 10(2): 194-199 (in Chinese).

[6] Aguiar F. C., Fernandes M. R., Ferreira M. T. et al. Riparian vegetation metrics as tools for guiding ecological restoration in riverscapes [J]. *Knowledge and Management of Aquatic Ecosystems*, 2011, 402: 251-264.

[7] Dijkstra J., Uittenbogaard R., Modeling the interaction between flow and highly flexible aquatic vegetation [J]. *Water Resources Research*, 2010, 46(12): W12547.

[8] Etminan V., Lowe R. J., Ghisalberti M. A new model for predicting the drag exerted by vegetation canopies [J]. *Water Resources Research*, 2017, 53(4): 3179-3196.

[9] Konings A. G., Katul G. G., Thompson S. E. A phenomenological model for the flow resistance over submerged vegetation [J]. *Water Resources Research*, 2012, 48(2): W02522.

[10] Abdelrhman M. A. Effect of eelgrass Zostera marina canopies on flow and transport [J]. *Marine Ecology Progress Series*, 2003, 248: 67-83.

[11] Abdelrhman M. A. Modeling coupling between eelgrass Zostera marina and water flow [J]. *Marine Ecology Progress Series*, 2007, 338(24): 81-96.

[12] Yang L. H., Zhuo L. H. Studies on purification ability of aquatic plants of the eutrophication water [J]. *Journal of Jilin Agricultural University*, 2006, 28(6): 663-666(in Chinese).

[13] Vance C. P. Symbiotic nitrogen fixation and phosphorus acquisition. Plant nutrition in a world of declining renewable resources [J]. *Plant Physiology*, 2001, 127(2): 390-397.

[14] Chen G., Huai W. X., Zhao M. D. Flow structure inpartially vegetated rectangular channels [J]. *Journal of Hydrodynamics*, 2010, 22(4): 590-597.

[15] Madsen J. D., Chambers P. A., James W. F. et al. The interaction between water movement, sediment dynamics and submersed macrophytes [J]. *Hydrobiologia*, 2001, 444(1-3